OPEN ACCESS
IOP Publishing
Superconductor Science and Technology
Supercond. Sci. Technol. **36** (2023) 075012 (8pp)
https://doi.org/10.1088/1361-6668/acd608

Significant improvement of the lower critical field in Y doped Nb: potential replacement of basic material for the radio-frequency superconducting cavity

Wei Xie, Yu-Hao Liu, Xinwei Fan and Hai-Hu Wen*

National Laboratory of Solid State Microstructures and Department of Physics, Collaborative Innovation Center of Advanced Microstructures, Nanjing University, Nanjing 210093, People's Republic of China

E-mail: hhwen@nju.edu.cn

Received 30 March 2023, revised 9 May 2023
Accepted for publication 16 May 2023
Published 12 June 2023

Abstract

The research of high energy and nuclear physics requires high power accelerators, and the superconducting radio-frequency (SRF) cavity is regarded as their engine. Up to now, the widely used practical and effective material for making the SRF cavity is pure Nb. The key parameter that governs the efficiency and the accelerating field (E_{acc}) of a SRF cavity is the lower critical field H_{c1}. Here, we report a significant improvement of H_{c1} for a new type of alloy, $Nb_{1-x}Y_x$ fabricated by the arc melting technique. Experimental investigations with multiple tools including x-ray diffraction, scanning electron microscopy, resistivity and magnetization are carried out, showing that the samples have good quality and a 30%–60% enhancement of H_{c1}. First principle calculations indicate that this improvement is induced by the delicate tuning of a Lifshitz transition of a Nb derivative band near the Fermi energy, which increases the Ginzburg–Landau parameter and H_{c1}. Our results may trigger a replacement of the basic material and thus a potential revolution for manufacturing the SRF cavity.

Supplementary material for this article is available online

Keywords: superconducting cavity, lower critical field, $Nb_{1-x}Y_x$ alloy, Ginzburg–Landau parameter

(Some figures may appear in colour only in the online journal)

* Author to whom any correspondence should be addressed.

1. Introduction

The superconducting radio-frequency (SRF) cavity was first proposed for accelerating charged particles and has been widely used for the study of high energy and nuclear physics [1]. A lot of research has been conducted on SRF cavities over the past decades. The performance of a state-of-the-art SRF cavity is mainly determined by two key parameters [2–4]: the quality factor Q and the accelerating gradient of the electric field E_{acc}. The quality factor Q is inversely proportional to the cavity radio-frequency (RF) surface resistance R_s as $Q = G/R_s$ (G is a geometrical factor independent of the cavity material) [2–5]. Generally, it is the energy loss in the skin layer of the cavity that restricts the RF application of superconductors when the RF electromagnetic wave is applied, and this power dissipation is characterized by the surface resistance R_s. Thus, Q determines the energy dissipation in the cavity per RF cycle. In principle, R_s is closely related to the normal state resistivity ρ_n (with the Bardeen-Cooper-Schrieffer theory in the dirty limit: $R_s \sim \sqrt{\rho_n}$) and the superconducting gap [2, 3]. The former measures the quasiparticle scattering rate and the latter influences the excited quasiparticle numbers at a certain temperature. In this case, Q can be evaluated by the normal state resistivity and the superconducting gap [2]. On the other hand, the maximal energy gained during each RF cycle is determined by E_{acc} which is proportional to the peak magnetic field B_{pk} in the way that $E_{acc} = B_{pk}/g$ (g is a factor dependent on the cavity shape, e.g. $g = 4.26$ mT MV^{-1} m for TESLA-shape cavity) [2, 4]. In principle, B_{pk} reflects the highest amplitude of the magnetic field for flux to penetrate the interior of the superconducting cavity. Thus, B_{pk} is limited by the maximum field for the superconductor to remain in the Meissner state and resist flux penetration. For type-I superconductors ($\kappa < 1/\sqrt{2}$, κ is the Ginzburg–Landau (GL) parameter), B_{pk} is limited by the thermodynamic critical field B_c, and for type-II superconductors ($\kappa > 1/\sqrt{2}$), B_{pk} is limited by the lower critical field B_{c1} [6, 7]. While in practice, due to the existence of surface Bean–Livingston barrier, the superconductor can hold the metastable Meissner state up to the superheating field B_{sh} ($>B_{c1}$) if the surface is very smooth [8–13]. B_{sh} is dependent both on the GL parameter κ and the thermodynamic critical field B_c. However, B_{sh} is difficult to reach in practice because of the surface roughness of the superconductor [14–16].

Up to now, Nb is still regarded as the most promising material for manufacturing the SRF cavities due to its relatively high critical temperature [2, 17], rather high lower-critical field B_{c1} [2, 9], large superfluid density among all the element or alloy superconductors, and the high residual resistivity ratio (RRR) [2, 18]. Meanwhile, its high ductility allows for easy manufacturing. However, in practical terms, the pure Nb cavity is approaching its fundamental limit in terms of the magnetic flux entry field B_{sh} [19–21], and it is highly desirable to have materials with better performance than Nb to make the SRF cavity [2, 9]. In order to improve the peak magnetic field or quality factor of a Nb cavity, some treatments have been carried out, such as the so-called International Linear Collider (ILC)recipe with the combination of the electro-polishing and baking at 120 °C for 48 h [22–25], nitrogen-doping [26–29], nitrogen-infusion [21, 30], Nb_3Sn coating [31–33], rare earth elements doping [34], etc. Some ideas for achieving higher energy barrier of flux entry were also proposed [2]. However, the improvement of B_{c1} due to the aforementioned methods is still very limited. Meanwhile, the multilayer-structure proposed by Gurevich [35, 36] and Kubo *et al* [37–39] has been under extensive research [40, 41]. The multilayer-structure consists of a superconducting and an insulating layer coated on the inner surface of the Nb cavity. The thickness of the superconducting layer should be in the scale of the London penetration depth, which is tens of nanometers for Nb [2]. These ideas definitely deserve to be tested, but they are technically very hard for manufacturing. Other candidate materials for SRF applications have also been explored, such as thin films of Nb [42, 43], NbN [3, 44], NbTiN [2], FeSe [45], MgB_2 [46] and some A15 compounds (Nb_3Sn, etc) coated on Nb or Cu substrates [47–49]. Besides the high demand for the quality factor and the peak magnetic field, the candidate materials for SRF applications also need to be tough, easy to refresh and polish. Thus, we focus on the manipulation of material properties by slightly doping other elements into Nb. Our goal is to increase the lower critical field, but maintain the high T_c, large RRR and toughness of Nb. After trying doping with many different elements, it is found that the $Nb_{1-x}Y_x$ alloys can achieve a lower critical field that is about 30%–60% higher than Nb. This shows the great potential for $Nb_{1-x}Y_x$ alloys to replace the existing Nb to achieve improved performance of the SRF cavity in the future.

2. Experimental details

The $Nb_{1-x}Y_x$ alloys were prepared by arc-melting method. Three doping levels were chosen, i.e. $x = 0.05$, 0.10, 0.15 for the $Nb_{1-x}Y_x$ alloys. The niobium (99.95%) and yttrium (99.9%), were weighed, ground and pressed into tablets to prepare the precursors according to the corresponding molar ratio in a glove box filled with argon. The precursors were then melted in an arc-furnace filled with high purity argon. The melting process lasts for at least 1 min. To improve the homogeneity of the ingots, all precursors were flipped and re-melted three times. Finally, well-mixed and high quality $Nb_{1-x}Y_x$ alloys were obtained. Structural characterization of the $Nb_{1-x}Y_x$ and Nb was performed with x-ray diffraction (XRD) measurements on a Bruker D8 Advanced diffractometer with the Cu-Kα radiation. The surface topography and element composition analysis of the $Nb_{1-x}Y_x$ and Nb were taken on a Phenom ProX scanning electron microscope (SEM).

For DC magnetization measurements, all the samples were cut into rectangular shapes by the wire cutting machine and carefully polished with sandpaper to obtain smooth and flat sample surfaces. The dimensions and weights of the bulks are $2.93 \times 2.90 \times 0.38$ mm^3 and 29.63 mg of $Nb_{0.95}Y_{0.05}$, $2.93 \times 2.87 \times 0.37$ mm^3 and 30.60 mg of $Nb_{0.9}Y_{0.1}$, $2.93 \times 2.85 \times 0.36$ mm^3 and 27.97 mg of $Nb_{0.85}Y_{0.15}$, $3.00 \times 2.70 \times 0.42$ mm^3 and 35.25 mg of Nb. The dimensions of $Nb_{1-x}Y_x$ and Nb are very close to each other, for the purpose of reducing the effect of the demagnetization

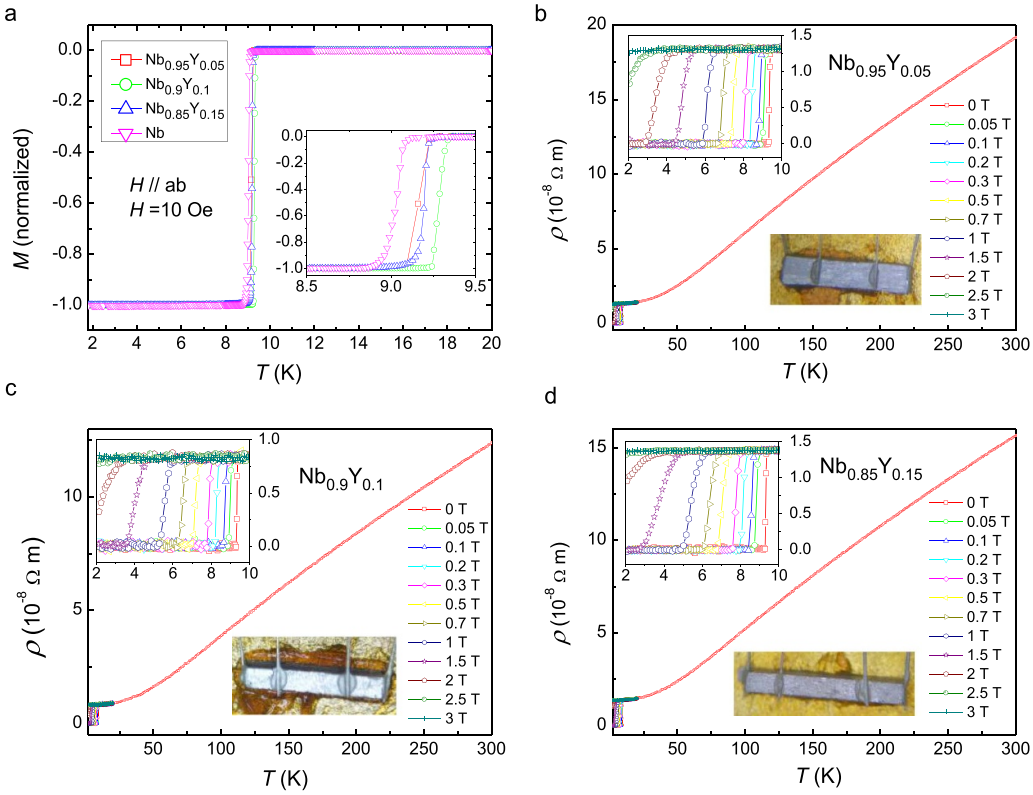

Figure 1. Temperature dependence of magnetization and resistive transport properties of the $Nb_{1-x}Y_x$ alloys. (a) Temperature dependence of magnetization measured in zero-field-cooled (ZFC) mode of the $Nb_{1-x}Y_x$ alloys and Nb. The magnetizations of all samples are normalized. The inset shows details of the magnetization curves $M(T)$ in the vicinity of T_c. Temperature dependence of resistivity of (b) $Nb_{0.95}Y_{0.05}$, (c) $Nb_{0.9}Y_{0.1}$, (d) $Nb_{0.85}Y_{0.15}$. Insets in (b)–(d) are enlarged views of resistivity at low temperatures. The images in (b)–(d) show the samples with electrodes for resistivity measurements.

Table 1. Superconducting parameters for the $Nb_{1-x}Y_x$ alloys and Nb. Including the critical temperature T_c, the lower critical field $H_{c1}(0)$, the upper critical field $H_{c2}(0)$, the GL parameter κ, the thermodynamic field $H_c(0)$ and the superheating field $H_{sh}(0)$. H_{c1} and H_{c2} of the different samples are fitted by the empirical formula $H(T) = H(0)[1 - (T/T_c)^2]^n$ to obtain $H_{c1}(0)$ and $H_{c2}(0)$ respectively, and the values in the brackets are the corresponding fitting parameters n. The GL parameter κ is calculated [62, 63] by $H_{c1}/H_{c2} = [\ln\kappa + \alpha(\kappa)]/(2\kappa^2)$, with $\alpha(\kappa) = 0.5 + \exp[-0.415\text{–}0.775\ \ln\kappa - 0.13(\ln\kappa)^2]$, and the H_{c1} and H_{c2} at 6 K are used in the calculation. The thermal dynamic field is calculated [62, 63] by $H_{c1}/H_c = [\ln\kappa + \alpha(\kappa)]/(\sqrt{2}\kappa)$. The superheating field is calculated [2, 12] by $H_{sh} = 1.26\ H_c$ ($\kappa \approx 1$).

Sample parameter	$Nb_{0.95}Y_{0.05}$	$Nb_{0.9}Y_{0.1}$	$Nb_{0.85}Y_{0.15}$	Nb
T_c (K)	9.22	9.35	9.24	9.17
$H_{c1}(0)$ (Oe)	1557 (1.22)	2055 (1.00)	1584 (0.98)	1267 (1.20)
$H_{c2}(0)$ (T)	1.60 (1.15)	1.71 (1.27)	1.52 (1.04)	0.87 (1.24)
κ	3.09	2.49	2.88	2.25
$H_c(0)$ (T)	0.37	0.43	0.36	0.25
$H_{sh}(0)$ (T)	0.47	0.54	0.45	0.31

factor. The DC magnetization measurements were carried out on a SQUID-VSM-7T (Quantum Design). Resistivity measurements were carried out on a physical property measurement system (PPMS 16T, Quantum Design), using the standard four-probe method.

3. Results and discussion

Alloys with three nominal doping levels have been prepared, they are $Nb_{0.95}Y_{0.05}$, $Nb_{0.9}Y_{0.1}$ and $Nb_{0.85}Y_{0.15}$. The doping ratio x of the $Nb_{1-x}Y_x$ alloys is the mole ratio of the precursor during preparation. A bulk sample of high-purity Nb is used for comparison. Figure 1(a) shows the temperature dependence of magnetization measured in the zero-field-cooled mode of $Nb_{1-x}Y_x$ and Nb. All samples are cut into a rectangular shape with almost the same sizes to reduce the interference of demagnetization effect [50, 51]. The applied magnetic field is 10 Oe and parallel to the lateral plane of the samples, which is defined as *ab*-plane. The superconducting transition temperature T_c is determined by the point where the magnetization starts to deviate from the paramagnetic background at high temperatures, and the results are summarized in table 1.

The $T_c = 9.35$ K of $Nb_{0.9}Y_{0.1}$ is a bit higher than $T_c = 9.17$ K of Nb and the T_c of $Nb_{0.95}Y_{0.05}$ and $Nb_{0.85}Y_{0.15}$ is extremely close. This indicates that the slight-doping of Y can slightly increase the T_c of Nb, which is consistent with previous results [52], and the operation temperature of SRF applications using the new alloy is guaranteed. The very steep magnetization transitions in figure 1(a) indicate a perfect Meissner shielding effect and the high quality of all samples. Thus, it is reliable to determine the lower critical field H_{c1} by the deviation from the linear Meissner line of the $M(H)$ curves when the field is parallel to the plane. Figures 1(b)–(d) show the temperature dependence of the electrical resistivity of $Nb_{1-x}Y_x$ with different nominal doping concentrations, respectively. The insets in figures 1(b)–(d) give details of the resistivity at low temperatures and the inserted images show the samples with electrodes for resistivity measurements. When the temperature decreases, the resistivity decreases monotonically and shows a metallic behavior before entering the superconducting state. Meanwhile, as the applied field increases, the transition of the resistivity widens slightly and shifts to lower temperatures until the superconductivity is suppressed completely. The RRR is related to the thermal conductivity of the material and is important for SRF cavities. The RRR of $Nb_{1-x}Y_x$ is defined as RRR $= \rho(300\text{ K})/\rho(10\text{ K})$. The measured results are RRR $= 14.5$ for $Nb_{0.95}Y_{0.05}$, RRR $= 14.9$ for $Nb_{0.9}Y_{0.1}$ and RRR $= 11.1$ for $Nb_{0.85}Y_{0.15}$, respectively. The RRR of $Nb_{1-x}Y_x$ is quite large, indicating the high quality of the samples, but these values are smaller than that of high-purity Nb (RRR $= 243$ in supplementary figure S4) [18]. This may be attributed to the slight doping of Y and the increase in impurity scattering. However, with heat treatment at high temperature, the RRR of $Nb_{1-x}Y_x$ may be further improved [52]. The temperature dependence of the electrical resistivity of our high-purity Nb is also given in supplementary figure S4.

The crystal structures of $Nb_{1-x}Y_x$ and Nb are examined by XRD and the XRD patterns are shown in figure 2(a). Nb has a cubic (bcc) symmetry and a space group of Im -3 m (number 229) [53]. The $Nb_{1-x}Y_x$ samples have the same index peaks as Nb and no other peaks can be observed in figure 2(a). This indicates that the $Nb_{1-x}Y_x$ samples have the same crystal structure as Nb and the slight doping with Y does not change the structure of Nb significantly. However, the (110) peaks of the XRD pattern of $Nb_{1-x}Y_x$ show a slight shift to a higher angle compared with Nb in the inset of figure 2(a). Meanwhile, the lattice parameters a calculated from the XRD patterns are 3.3065(3) Å for $Nb_{0.95}Y_{0.05}$, 3.3027(8) Å for $Nb_{0.9}Y_{0.1}$ and 3.3095(9) Å for $Nb_{0.85}Y_{0.15}$, compared with 3.3167(5) Å for Nb. The slight decrease in lattice parameters and the shift of (110) peaks from the XRD patterns both indicate that a measurable amount of Y has been successfully incorporated into Nb. The energy dispersive spectrums (EDS) of $Nb_{1-x}Y_x$ and Nb from SEM measurements are shown in figure 2(b). The corresponding SEM images are given in supplementary figure S5. The SEM image in figure 2(b) shows a quite smooth surface of $Nb_{0.9}Y_{0.1}$ with no clear grain boundary. The inset in figure 2(b) shows an enlarged view of the EDS around 1.9 keV and the dashed vertical lines are the characteristic peaks of Nb

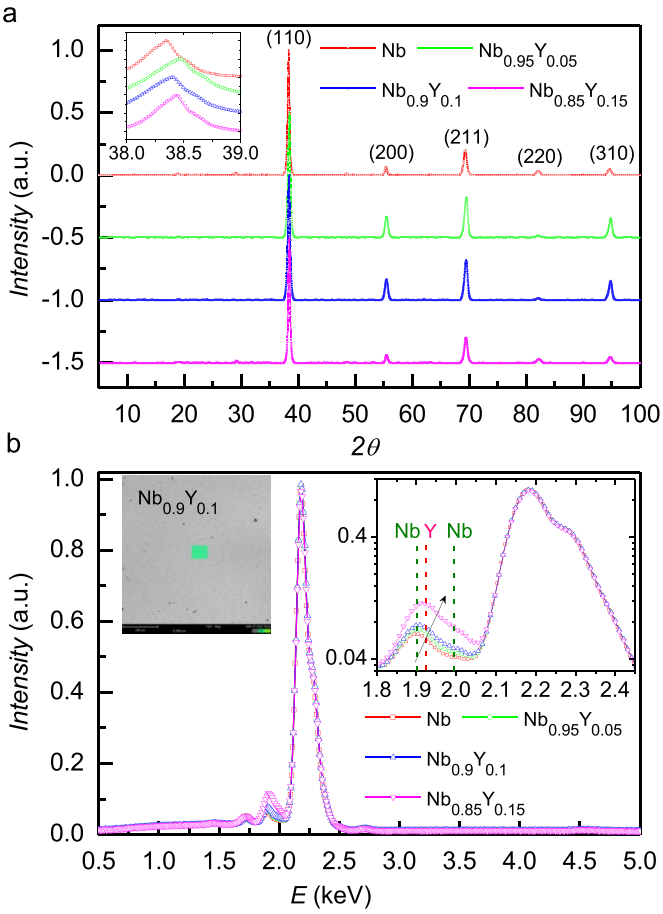

Figure 2. XRD, SEM image and energy dispersive spectrums (EDS) of the $Nb_{1-x}Y_x$ alloys and Nb. (a) XRD of the $Nb_{1-x}Y_x$ alloys and Nb. Inset is an enlarged view of the (110) peak in XRD patterns. (b) EDS of the $Nb_{1-x}Y_x$ alloys and Nb. The image is an SEM image of $Nb_{0.9}Y_{0.1}$ corresponding to the EDS measurement. Inset is the enlarged view of peaks around 1.9 keV in EDS, the dashed vertical lines are the characteristic peaks of Nb (olive) and Y (pink) in the vicinity, and the black arrow shows the elevation and high-energy shift of the peak, which is attributed to the existence of Y in the alloys.

(olive) and Y (pink) in the vicinity. With increasing ratio of Y in the alloys, the peak around 1.9 keV is elevated and shifts to higher energy, which is indicated by the black arrow in the inset of figure 2(b). This confirms the existence of Y in the alloys and the atomic compositions of Y from EDS analyses are 1.14% for $Nb_{0.95}Y_{0.05}$, 1.82% for $Nb_{0.9}Y_{0.1}$ and 5.46% for $Nb_{0.85}Y_{0.15}$. This shows a loss of Y in the $Nb_{1-x}Y_x$ alloys compared to the nominal composition of the starting materials and may be attributed to a saturation of the solubility of Y in Nb, which is consistent with previous results [52]. Even within this solution limit, an increase of the lower critical field of the alloys can be clearly seen.

Figures 3(a)–(c) show the isothermal magnetic-hysteresis-loops (MHLs) of $Nb_{1-x}Y_x$ and Nb measured at the same temperature, respectively. The temperature ranges from 2 K to 6 K and the magnetic field ranges from -1 T to 1 T. The field is parallel to the *ab*-plane of the samples, for the purpose of reducing the influence of the demagnetization effect [50, 51].

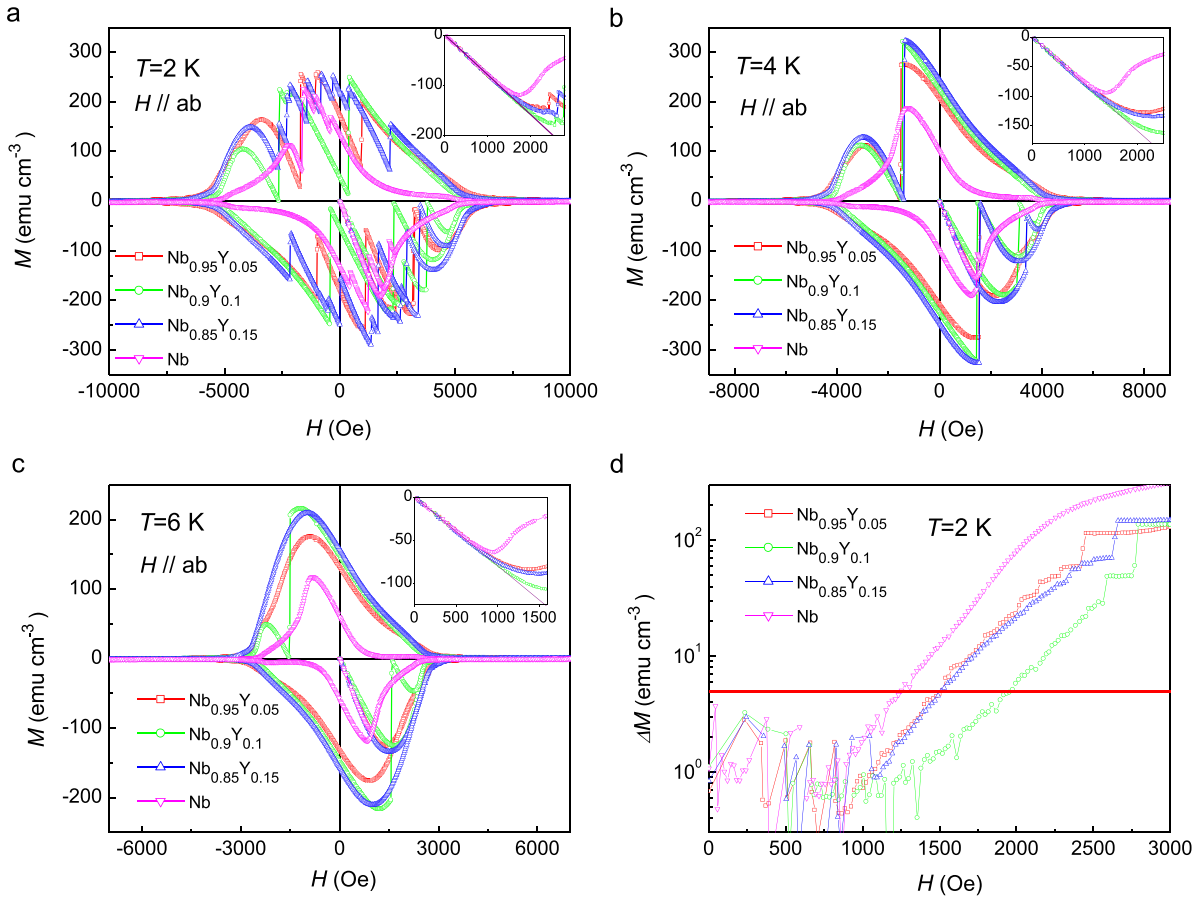

Figure 3. MHLs and determination of H_{c1} for the $Nb_{1-x}Y_x$ alloys and Nb. MHLs of the $Nb_{1-x}Y_x$ alloys and Nb at: (a) 2 K, (b) 4 K, (c) 6 K. Insets in (a)–(c) are enlarged views of the Meissner state and the initial penetration stage at low fields, the magnetizations of different samples are normalized. (d) The deviation of the initial penetration magnetization with respect to the corresponding Meissner line at 2 K. The criterion used to determine H_{c1} is $\Delta M = 5$ emu cm^{-3} (red horizontal line).

The MHLs of $Nb_{1-x}Y_x$ show stronger symmetric features with respect to the horizontal line than that of Nb, and this indicates a stronger bulk flux pinning of the alloy [51]. The avalanche-like flux jump effect with the flux abruptly entering the sample can be seen in $Nb_{1-x}Y_x$, which is closely related to the thermomagnetic instabilities of the critical state, and it becomes more obvious at low temperatures [54, 55]. However, this 'harmful' flux jump only occurs when the vortices begin to penetrate the sample, thus it may not affect the SRF applications which work mainly in the Meissner state [2, 4, 9]. On the other hand, the flux trapped during the cooling process significantly degrades the quality factor Q. Understanding the tendency of flux trapping in $Nb_{1-x}Y_x$ and its sensitivity is one of the tasks for the future [56, 57]. The insets in figures 3(a)–(c) present details of the Meissner state of the initial $M(H)$ curves in the low-field region. It should be pointed out that, the magnetization has been corrected to make $M(H)$ curves of the Meissner state of different samples merge into one line. Through comparison of the initial $M(H)$ curves, it can be seen that the $Nb_{1-x}Y_x$ can hold the Meissner state (the linear part of $M(H)$ curves) to a higher field than Nb, and among them the $Nb_{0.9}Y_{0.1}$ sample shows the best performance. The lower critical field H_{c1} is defined as where the $M(H)$ curve starts to deviate from the linear line. To obtain the value of H_{c1} precisely, the deviation from the linear Meissner line of the $M(H)$ curve has been calculated accurately for each sample [58, 59]. Firstly, the linear Meissner line is obtained by fitting to the linear part of $M(H)$ curve in the low-field region. Due to the small difference in sample size, the linear Meissner lines of $Nb_{1-x}Y_x$ and Nb are slightly different. Secondly, we subtract the corresponding Meissner lines from the initial $M(H)$ curves and the deviation of magnetization can then be obtained. The same criterion of $\Delta M = 5$ emu cm^{-3} is used to determine the value of H_{c1} for all temperatures, as it is comparable to the background signal. The deviation of magnetization at 2 K for $Nb_{1-x}Y_x$ and Nb are shown in figure 3(d) and the red horizontal line is the criterion of magnetization for determining the H_{c1}. The obtained results from figure 3(d) are $H_{c1}(2\text{ K}) = 1515$ Oe of $Nb_{0.95}Y_{0.05}$, $H_{c1}(2\text{ K}) = 1953$ Oe of $Nb_{0.9}Y_{0.1}$, $H_{c1}(2\text{ K}) = 1509$ Oe of $Nb_{0.85}Y_{0.15}$ and $H_{c1}(2\text{ K}) = 1247$ Oe of Nb. The H_{c1} of $Nb_{0.9}Y_{0.1}$ is 57% higher than that of Nb and gives rise to the strongest enhancement, and all three alloys show a clear improvement of H_{c1} compared to Nb. The determination of H_{c1} at other temperatures is given in supplementary figure S1 and supplementary table S1.

Figure 4(a) shows the temperature dependence of the lower critical field H_{c1} of $Nb_{0.9}Y_{0.1}$, $Nb_{0.85}Y_{0.15}$ and Nb. In order to obtain the values of H_{c1} at zero temperature, the empirical

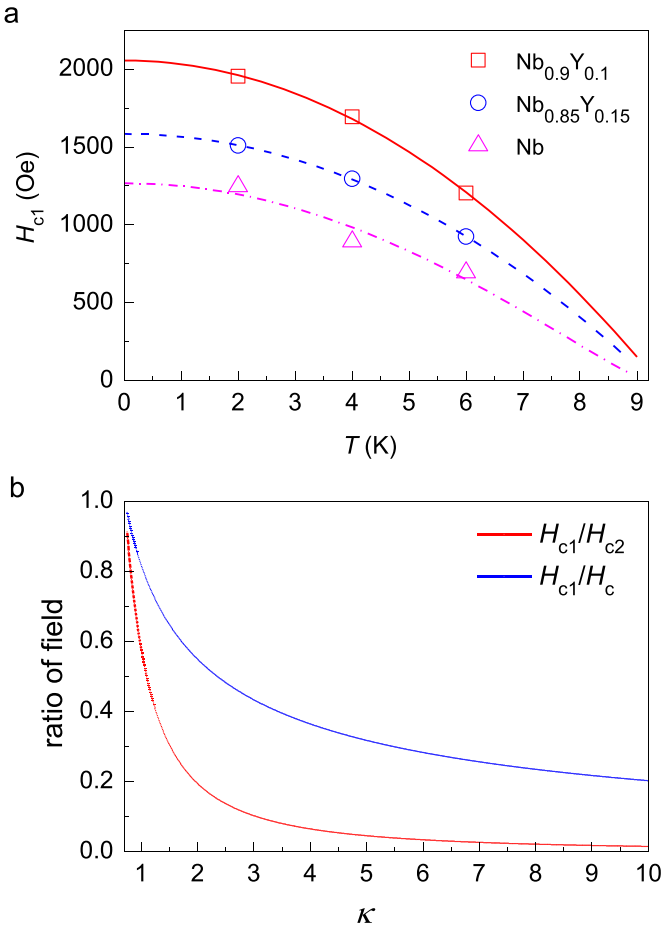

Figure 4. The lower critical field H_{c1} of the $Nb_{1-x}Y_x$ alloys and Nb in our experiment. All H_{c1} values are determined from the deviating point of the $M(H)$ curve from the linear Meissner line. (a) Temperature dependence of the lower critical field H_{c1} of the $Nb_{1-x}Y_x$ alloys and Nb. The lines are the corresponding fitting curves using the empirical formula $H(T) = H(0)[1 - (T/T_c)^2]^n$. The fitting parameters are $n = 1.00$ of $Nb_{0.9}Y_{0.1}$, $n = 0.98$ of $Nb_{0.85}Y_{0.15}$ and $n = 1.20$ of Nb. (b) The κ dependence of the ratio of critical field from theoretical calculation [62, 63] given by $H_{c1}/H_{c2} = [\ln\kappa + \alpha(\kappa)]/(2\kappa^2)$ and $H_{c1}/H_c = [\ln\kappa + \alpha(\kappa)]/(\sqrt{2}\kappa)$, $\alpha(\kappa) = 0.5 + \exp[-0.415\text{–}0.775\ \ln\kappa - 0.13(\ln\kappa)^2]$.

formula $H(T) = H(0)[1 - (T/T_c)^2]^n$ is used to fit the $H_{c1}(T)$ of all samples and the fitting curves are shown in figure 4(a), respectively. The fitting parameters are $n = 1.00$ of $Nb_{0.9}Y_{0.1}$, $n = 0.98$ of $Nb_{0.85}Y_{0.15}$ and $n = 1.20$ of Nb, and are summarized in table 1. $H_{c1}(0) = 2055$ Oe of $Nb_{0.9}Y_{0.1}$ is the highest value and 62% higher than $H_{c1}(0) = 1267$ Oe of Nb (table 1). Concerning the values of $H_{c1}(0)$ for pure Nb reported in literatures [2, 9, 60], there are clear discrepancies. The often cited value of $H_{c1}(0) = 1700$ Oe was adopted from [60], while we find that the authors there used the full penetration field on the MHL as the H_{c1}, not the deviating point of the $M(H)$ curve from the linear Meissner line. In another report with samples of Nb single crystals, the H_{c1} at 1.83 K is smaller than 1235 Oe. This is close to our values. If taking the full penetration field as H_{c1} that would give a value beyond 2500 Oe ($T = 2$ K) for the sample $Nb_{0.9}Y_{0.1}$. We believe that an appropriate post-annealing of our Nb samples may increase the $H_{c1}(0)$ value further. However, in any case, this value is smaller than that in the Y doped samples. For the Nb samples with polished surfaces, we find that the $H_{c2}(0)$ values determined from the resistive onset transition temperature are quite high ($\geqslant$1.5 T) and much larger than that from other literatures [2, 8, 42], we believe that this is probably due to the surface superconductivity. Thus, we use the temperature dependent magnetization, which usually reflects the bulk properties, to determine the upper critical field H_{c2} (supplementary figures S2 and S3). The empirical formula $H(T) = H(0)[1 - (T/T_c)^2]^n$ is used to fit the H_{c2} of all samples to extrapolate $H_{c2}(0)$ (supplementary figure S3). The $H_{c2}(0)$ of $Nb_{1-x}Y_x$ is twice that of Nb (table 1). The clear enhancement of H_{c1} in Y-doped Nb is of great significance for the application of the alloy. Above all, the new alloys $Nb_{1-x}Y_x$ can serve as a promising candidate material for SRF applications.

In order to study the physical reason for the improved H_{c1} in $Nb_{1-x}Y_x$ compared with Nb, we carry out first principle calculations. Figure 5(a) illustrates the calculated band structure of Nb. There are both hole and electron pockets near the Γ point of the band structure of Nb. When the doping level of the alloy is changed, the Fermi level moves up and down and a Lifshitz transition can occur. This Lifshitz transition occurs most likely for the band between N-Γ in which a band bottom appears very close to the Fermi energy. Figure 5(b) illustrates the total density of states (DOS) of Nb, which consists of the DOS of both p orbit and d orbit. It can be seen that, the DOS of d orbit accounts for the main part of the total DOS of Nb. There is a sharp peak of DOS at slightly negative energy side. This is induced by the shallow band bottom between N-Γ. If doping with holes in Nb (the substitution of Nb by Y is hole doping), the Fermi energy will drop down (the zero energy point moves left in figure 5(b)), and thus the DOS will increase to a higher value (the sharp peak on the left of the zero energy point in figure 5(b)). Figure 5(c) illustrates the three-dimensional (3D) Fermi surface of Nb with color-coded Fermi velocities, and the first Brillouin zone of Nb has the symmetry of a dodecahedron. In principle, the coherence length ξ can be written as $\xi = \hbar v_F/\pi\Delta$, where v_F is the Fermi velocity, Δ is the superconducting gap and $\hbar$ is the reduced Planck constant. The superconducting gap remains almost the same for the alloys compared with Nb and so is ξ. On the other hand, the condensed carrier density n_s/m^* can be written as $n_s/m^* = \sigma/e^2\tau \propto \sigma/\tau$, where n_s is the superconducting carrier density, m^* is the effective mass, σ is the conductivity and τ is the relaxation time. As illustrated in figure 5(d), the condensed carrier density of Nb decreases with slight doping of Y into Nb (hole-doping). The London penetration depth λ can be written as $\lambda = (m^*/\mu_0 n_s e^2)^{1/2}$ and therefore increases slightly [61]. For these reasons, the GL parameter $\kappa = \lambda/\xi$ increases.

In the case of small κ value, the vortex core should be taken into consideration in evaluating the vortex tension energy and the lower critical field. Thus, through theoretical calculation given by Brandt [62, 63], the κ dependence of the

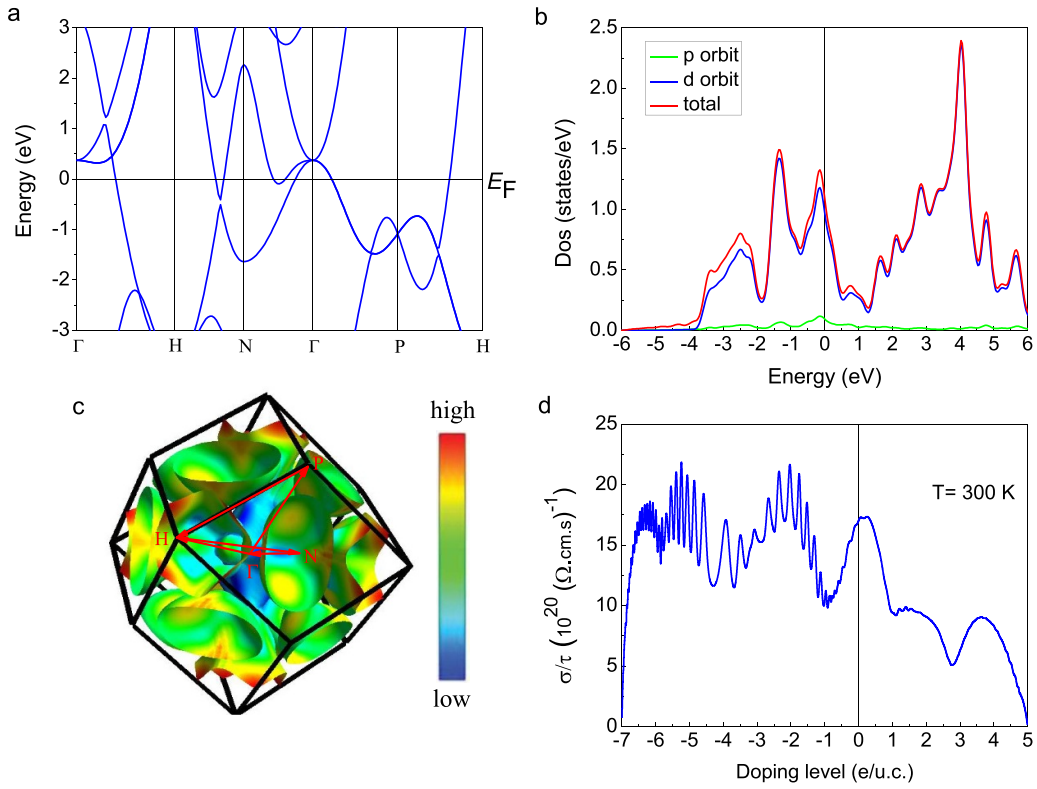

Figure 5. First principle calculations of the electronic structure of Nb. (a) Band structure of Nb. (b) Density of states (DOS) of Nb, including the total DOS (red line), the DOS of *p* orbit (green line) and *d* orbit (blue line). (c) 3D Fermi surface of Nb with color-coded Fermi velocities (blue is low and red is high velocity). (d) The ratio of conductivity and relaxation time σ/τ as a function of doping level for Nb at 300 K.

ratio of the critical field is $H_{c1}/H_{c2} = [\ln\kappa + \alpha(\kappa)]/(2\kappa^2)$, $\alpha(\kappa) = 0.5 + \exp[-0.415\text{–}0.775\ \ln\kappa - 0.13(\ln\kappa)^2]$. The curve is shown in figure 4(b) and the κ ranges from 0.75 to 10. The above formulae are valid when T is close to T_c. Therefore, we use the H_{c1} and H_{c2} at 6 K to calculate the value of κ. The results are $\kappa = 3.09$ of $Nb_{0.95}Y_{0.05}$, $\kappa = 2.49$ of $Nb_{0.9}Y_{0.1}$, $\kappa = 2.88$ of $Nb_{0.85}Y_{0.15}$ and $\kappa = 2.25$ of Nb. The thermodynamic critical field H_c is given [62, 63] by $H_{c1}/H_c = [\ln\kappa + \alpha(\kappa)]/(\sqrt{2}\kappa)$ in figure 4(b) and the superheating field H_{sh} is determined by $H_{sh} = 1.26\ H_c$ ($\kappa \approx 1$) [12]. For the samples studied here, we have calculated different quantities and the results are summarized in table 1. The κ of $Nb_{1-x}Y_x$ is higher than that of Nb (table 1), and the latter is higher than the values for Nb from other literatures ($\kappa \sim 1$) [2, 9]. To deal with this difference, we use the full penetration field as the criteria of H_{c1} as adopted by others [60], and we have $H_{c1}(6\text{ K}) = 955$ Oe of Nb. With the upper critical field $H_{c2}(6\text{ K}) = 0.43$ T of Nb and the Brandt's formula for H_{c1}/H_{c2}, we have $\kappa = 1.80$ of Nb. This value of κ is much closer to 1. The RRR value is often used to estimate the κ of Nb and we have $\kappa/\kappa_0 = 1.06$ for RRR = 243 in our experiment, where κ_0 is the GL parameter for the pure material [64]. The value of 1.06 is close to that of ideal pure Nb [64]. The $H_c(0)$ of Nb is close to the values from other literatures ($H_c(0) \sim 0.2$ T) [65, 66], which reflects the bulk properties of superconductors. With the slight Y doping, the H_{c2} of $Nb_{1-x}Y_x$ is elevated a lot compared with the pure Nb (table 1). Due to both the increase of H_{c2} and κ, the lower critical field H_{c1} is increased as well. Among all the alloys, $Nb_{0.9}Y_{0.1}$ gives rise to the highest value of $H_{c2}(0)$ (=1.71 T) and an increase of κ (=2.49), and therefore the highest improvement of $H_{c1}(0)$ (=2055 Oe). This is consistent with our theoretical argument. Again, we want to emphasize that the $H_{c1}(T)$ here are all determined from the very first deviating point of the $M(H)$ curve from the Meissner linear line. Meanwhile, $H_{sh}(0)$ of $Nb_{1-x}Y_x$ is higher than that of Nb in our study, and approaches that of Nb_3Sn [2, 9, 38]. All these indicate the promising potential of $Nb_{1-x}Y_x$ for SRF applications.

4. Conclusions

We report systematic investigations on a new type of alloy $Nb_{1-x}Y_x$ prepared by arc melting method. The lower critical field H_{c1} of $Nb_{1-x}Y_x$ is found to be 30%–60% higher than that of high-purity Nb. This may greatly improve the accelerating gradient of the electric field E_{acc} for a superconducting cavity. Thus, the $Nb_{1-x}Y_x$ alloy may serve as a promising candidate for replacing Nb in SRF cavity applications.

Data availability statement

All data that support the findings of this study are included within the article (and any supplementary files).

Acknowledgments

We appreciate the useful discussions with Peng Sha and Chao Dong in Institute of High Energy Physics, CAS. We would also like to thank Alex Gurevich at Old Dominion University for useful discussions. This work is supported by the National Natural Science Foundation of China (Grant Nos. A0402/11927809 and A0402/11534005), National Key R and D Program of China (Grant No. 2022YFA1403201), and the Strategic Priority Research Program of Chinese Academy of Sciences (Grant No. XDB25000000).

ORCID iDs

Wei Xie https://orcid.org/0000-0002-8194-6433
Xinwei Fan https://orcid.org/0000-0003-2283-6266
Hai-Hu Wen https://orcid.org/0000-0003-0093-1625

References

[1] Banford A P and Stafford G H 1961 *J. Nucl. Energy* C **3** 287
[2] Valente-Feliciano A 2016 *Supercond. Sci. Technol.* **29** 113002
[3] Antoine C Z, Aburas M, Four A, Weiss F, Iwashita Y, Hayano H, Kato S, Kubo T and Saeki T 2019 *Supercond. Sci. Technol.* **32** 085005
[4] Gurevich A 2017 *Supercond. Sci. Technol.* **30** 034004
[5] Gurevich A and Kubo T 2017 *Phys. Rev. B.* **96** 184515
[6] Abrikosov A A 1957 *J. Exp. Theor. PhyS. U. S. S. R.* **32** 1442
[7] Ginzburg V L and Landau L D 1950 *Zh. Eksp. Teor. Fiz.* **20** 1064
[8] Bean C P and Livingston J D 1964 *Phys. Rev. Lett.* **12** 14
[9] Liarte D B, Posen S, Transtrum M K, Catelani G, Liepe M and Sethna J P 2017 *Supercond. Sci. Technol.* **30** 033002
[10] Lin F P J and Gurevich A 2012 *Phys. Rev. B.* **85** 054513
[11] Kubo T 2020 *Phys. Rev. Res.* **2** 033203
[12] Dolgert A J *et al* 1996 *Phys. Rev. B.* **53** 5650
[13] Transtrum M K, Catelani G and Sethna J P 2011 *Phys. Rev.* B **83** 094505
[14] Buzdin A and Daumens M 1998 *Physica* C **294** 257
[15] Aladyshkin A Y, Mel'nikov A S, Shereshevsky I A and Tokman I D 2001 *Physica* C **361** 67
[16] Kubo T 2015 *Prog. Theor. Exp. Phys.* **2015** 063G01
[17] Bieler T R *et al* 2010 *Phys. Rev. ST Accel. Beams* **13** 031002
[18] Liu B *et al* 2021 *Nucl. Instrum. Methods Phys. Res.* A **993** 165080
[19] Geng R L *et al* 2007 *Proc. of PAC07* (Albuquerque, NM: JACoW, CERN Geneva) p 2337
[20] Kubo T *et al* 2014 *Proc. IPAC2014* (Dresden: JACoW, CERN Geneva) p 2519
[21] Grassellino A *et al* 2017 *Supercond. Sci. Technol.* **30** 094004
[22] Saito K *et al* 1997 *Proc. of SRF1997* (Abano Terme: JACoW, CERN Geneva) p 795
[23] Lilje L *et al* 1999 *Proc. SRF1999* (La Fonda Hotel, Santa Fe, NM: JACoW, CERN Geneva) p 74
[24] Romanenko A, Grassellino A, Barkov F and Ozelis J P 2013 *Phys. Rev. Spec. Top. Accel. Beams* **16** 012001
[25] Romanenko A, Grassellino A, Barkov F, Suter A, Salman Z and Prokscha T 2014 *Appl. Phys. Lett.* **104** 072601
[26] Grassellino A, Romanenko A, Sergatskov D, Melnychuk O, Trenikhina Y, Crawford A, Rowe A, Wong M, Khabiboulline T and Barkov F 2013 *Supercond. Sci. Technol.* **26** 102001
[27] Dhakal P *et al* 2013 *Phys. Rev. Spec. Top. Accel. Beams* **16** 042001
[28] Yang L *et al* 2021 *Nanotechnology* **32** 245701
[29] Lechner E M, Oli B D, Makita J, Ciovati G, Gurevich A and Iavarone M 2020 *Phys. Rev. Appl.* **13** 044044
[30] Martinello M, Checchin M, Romanenko A, Grassellino A, Aderhold S, Chandrasekeran S K, Melnychuk O, Posen S and Sergatskov D A 2018 arXiv:1806.09824
[31] Posen S and Hall D L 2017 *Supercond. Sci. Technol.* **30** 033004
[32] Keckert S *et al* 2019 *Supercond. Sci. Technol.* **32** 075004
[33] Posen S, Lee J, Seidman D N, Romanenko A, Tennis B, Melnychuk O S and Sergatskov D A 2021 *Supercond. Sci. Technol.* **34** 025007
[34] Jiang T, He F-S, Jiao F, He F, Lu X-Y, Zhao K, Zhao H-Y, You Y-S and Chen L 2014 *Chin. Phys.* B **23** 057403
[35] Gurevich A 2006 *Appl. Phys. Lett.* **88** 012511
[36] Gurevich A 2015 *AIP Adv.* **5** 017112
[37] Kubo T, Iwashita Y and Saeki T 2014 *Appl. Phys. Lett.* **104** 032603
[38] Kubo T 2017 *Supercond. Sci. Technol.* **30** 023001
[39] Kubo T 2021 *Supercond. Sci. Technol.* **34** 045006
[40] Ito H, Watanabe A, Morimoto Y, Nakagawa K, Nishii N, Nakamura K, Morita H and Ito H 2019 *Proc. SRF2019* (Dresden (JACoW, CERN Geneva) p 632
[41] Katayama R *et al* 2019 *Proc. SRF2019* (Dresden: JACoW, CERN Geneva) p 807
[42] Ries R, Seiler E, Gömöry F, Medvids A, Onufrijevs P, Pira C, Chyhyrynets E, Malyshev O B and Valizadeh R 2021 *Supercond. Sci. Technol.* **34** 065001
[43] Valente-Feliciano A *et al* 2021 arXiv:2204.02536
[44] Leith S, Vogel M, Fan J, Seiler E, Ries R and Jiang X 2021 *Supercond. Sci. Technol.* **34** 025006
[45] Lin Z *et al* 2021 *Supercond. Sci. Technol.* **34** 015001
[46] Tan T, Wolak M A, Xi X X, Tajima T and Civale L 2016 *Sci. Rep.* **6** 35879
[47] Sharma R G 1987 *Cryogenics* **27** 361–78
[48] Stewart G R 2015 *Physica* C **514** 28–35
[49] Barzi E *et al* 2021 arXiv:2203.09718
[50] Prozorov R and Kogan V G 2018 *Phys. Rev. Applied* **10** 014030
[51] Xie W, Liu Y H and Wen H H 2022 *Phys. Rev. B.* **105** 014505
[52] Koch C C and Kroeger D M 1975 *J. Less-Common Met.* **40** 29–38
[53] Seybolt A U 1954 *JOM* **6** 774–6
[54] Evetts J E, Campbell A M and Dew-hughes D 1964 *Phil. Mag.* **10** 339–43
[55] Tsindlekht M I, Genkin V M, Felner I, Zeides F, Katz N, Gazi Š and Chromik Š 2014 *Phys. Rev. B.* **90** 014514
[56] Romanenko A, Grassellino A, Crawford A C, Sergatskov D A and Melnychuk O 2014 *Appl. Phys. Lett.* **105** 234103
[57] Huang S, Kubo T and Geng R 2016 *Phys. Rev. Accel. Beams* **19** 082001
[58] Liang R, Bonn D A, Hardy W N and Broun D 2005 *Phys. Rev. Lett.* **94** 117001
[59] Ren C, Wang Z S, Luo H Q, Yang H, Shan L and Wen H H 2008 *Phys. Rev. Lett.* **101** 257006
[60] Finnemore D K, Stromberg T F and Swenson C A 1966 *Phys. Rev.* **149** 231
[61] London F and London H 1935 *Proc. R. Soc.* A **155** 71
[62] Brandt E H 2003 *Phys. Rev.* B **68** 054506
[63] Gurevich A 2012 *Rev. Accel. Sci. Technol.* **05** 119
[64] Ooi S, Tachiki M, Konomi T, Kubo T, Kikuchi A, Arisawa S, Ito H and Umemori K 2021 *Phys. Rev. B.* **104** 064504
[65] Mcconville T and Serin B 1965 *Phys. Rev.* **140** A1169
[66] Junod A, Jorda J L and Muller J 1986 *J. Low Temp. Phys.* **62** 301